

Contribution of Unresolved Point Sources to the Diffuse X-ray Background below 1 keV

A. Gupta, and M. Galeazzi¹

Physics Department, University of Miami, Coral Gables, FL 33124

ABSTRACT

We present here the analysis of X-rays point sources detected in several observations available in the XMM-Newton public archive. We focused, in particular, on energies below 1 keV, which are of particular relevance to the understanding of the Diffuse X-ray Background. The average field of all the exposures is 0.09 deg^{-2} . We reached an average flux sensitivity of $5.8 \times 10^{-16} \text{ erg s}^{-1} \text{ cm}^{-2}$ in the soft band (0.5-2.0 keV) and $2.5 \times 10^{-16} \text{ erg s}^{-1} \text{ cm}^{-2}$ in the very soft band (0.4-0.6 keV). In this paper we discuss the logN-logS results, the contribution to the integrated X-ray sky flux, and the properties of the cumulative spectrum from all sources. In particular, we found an excess flux at around 0.5 keV in the composite spectrum of faint sources. The excess seems to be a general property of all the fields observed suggesting an additional class of weak sources is contributing to the X-ray emission at these energies. Combining our results with previous investigations we have also quantified the contribution of the individual components of the diffuse X-ray Background in the 3/4 keV band.

Subject headings: X-rays: diffuse background

1. Introduction

The existence of a Diffuse X-ray Background (*DXB*) was one of the first discoveries of extrasolar X-ray astronomy (Giacconi et al. 1962). In the intervening decades, observations with improving angular and spectral resolution have enhanced our understanding of the components that make up this background. Above 1 keV, the emission is highly isotropic on large angular scales, has extragalactic origin, and can be fully accounted by the superposition of unresolved point sources (Mushotzky et al. 2000). Below 1 keV, the *DXB* is a mixture

¹corresponding author, galeazzi@physics.miami.edu

of the Galactic diffuse emission from a hot bubble surrounding the solar neighborhood (the Local Bubble, LB), charge exchange from solar wind ions (*SWCX*), hot gas in the galactic halo, and an extragalactic flux from point sources and from intercluster warm gas that may contain the bulk of the present day baryons (Cen & Ostriker 1999; Ursino & Galeazzi 2006; Galeazzi et al. 2009). Analyses of the soft X-ray background (below 1 keV) usually model the Local Bubble component as unabsorbed plasma thermal emission, the hotter Galactic halo emission as multiple plasma thermal components absorbed by the gas in the Galactic disk, and the unresolved extragalactic sources component (primarily active galactic nuclei - *AGN*), with an absorbed power law, which is often an extension of the power law fit derived at higher energy (Gendreau et al. 1995; McCammon et al. 2002).

Recent investigations have attempted to separate the various components by using shadow experiments and other observational techniques (Galeazzi et al. 2007; Smith et al. 2006; Henley & Shelton 2008), however such experiments only separate the various components into two major groups, foreground and background, and rely on understanding the spectral properties of the different components to fully separate them. The contribution of unresolved point sources to the *DXB* dominates above 1 keV and is still significant at lower energies. A good understanding of its properties, beyond the extension of higher energy investigations, is therefore critical for any investigation of the *DXB*. This, however, is made difficult by the characteristics of current X-ray missions, as high angular resolution missions such as Chandra¹, designed for good source identification, have a relatively limited response in the energy range of interest, while missions designed for good response in the low energy range, such as the XQC program (McCammon et al. 2002), lack the necessary angular resolution. XMM-Newton, while not optimized for such an investigation, is a good compromise of angular resolution and response below 1 keV, and has been used in our investigation.

2. Data Reduction

2.1. Data preparation

We used the data from 10 observations, corresponding to 5 different targets available in the XMM-Newton public archive. The choice of the targets was based on several considerations. To limit the effect of absorption from the neutral hydrogen and contamination from galactic emission we used targets at least 30° above the galactic plane and with neutral hydrogen densities smaller than $2.0 \times 10^{20} \text{ cm}^{-2}$. To have significant statistics we also limited

¹http://cxc.harvard.edu/cdo/about_chandra/overview_cxo.html/

the investigation to targets with at least 80,000 seconds of good observing time. The targets used and their characteristics are summarized in Table 1.

Data from the full XMM-Newton field of view were used in the analysis. The raw data were processed using the Standard Analysis Software (*SAS*)². Events spread at most in two contiguous pixels for the *PN* (i.e., pattern=0-4) and in four contiguous pixels for the *MOS* (i.e., pattern=0-12) have been selected. Event files were cleaned of bad pixels (hot pixels, events out of the field of view, etc.) and soft proton flares. The soft proton flares are due to protons with energies less than a few hundred keV. The flares can produce a count rate up to a factor 100 greater than the mean stationary background count rate. They are variable during an observation and from observation to observation, and do not have a predictable spectral shape or spatial distribution on the detector (Read & Ponman 2003). In order to remove periods of unwanted high background levels, we rejected the times with a 0.5-10 keV count rate higher than 8 counts s⁻¹ for the *PN* and 3 counts s⁻¹ for each of the two *MOS* cameras. Multiple observations of the same XMM-Newton targets were added using *SAS* task *merge*.

2.2. Source Detection

The clean event files were used to generate *MOS1*, *MOS2*, and *PN* images in the 0.4-0.6 keV and 0.5-2.0 keV bands. A corresponding set of exposure maps was generated to account for spatial quantum efficiency, mirror vignetting, and field of view of each instrument by running XMM-SAS task *exppmap*. This task evaluates the above quantities assuming an event energy that corresponds to the mean of the energy band boundaries.

The excellent relative astrometry between the three cameras (within 1", well under the *FWHM* of the Point Spread Function - *PSF*) allowed us to merge together the *MOS* and *PN* images in order to increase the signal-to-noise ratio of the sources and reach fainter X-ray fluxes; the corresponding exposure maps were merged as well. The source detection and characterization procedure applied to the image sets involved the creation of a background map for each energy band. As a first step, the XMM-SAS sliding cell detection algorithm *eboxdetect* was run in local detection mode. In this procedure source counts were collected in the cells of 5 × 5 pixels adopting a low threshold in the detection likelihood to produce a source list. The XMM-SAS task *esplinemap* removed from the original merged image within a radius of 1.5 times the *FWHM* of the *PSF* all the sources in the list and creates the so-called "*cheesed*" image and a mask image with value unity in each pixel outside the source

²<http://xmm.vilspa.esa.es/sas/>

circles and zero within. We then flat-fielded the cheesed images by dividing them by the exposure maps and smoothed them with a Gaussian of $5'$ *FWHM* using *SAS* task *asmooth*. The masked images were also smoothed with the same Gaussian as the actual image data. Finally, background maps were calculated by dividing the smoothed cheese images by the smoothed mask images. The result was multiplied by the exposure maps. An example of background map of the Lockman Hole is shown in Figure 1.

Using the calculated background maps, *eboxdetect* was run in map detection mode to identify point sources. In map detection mode the background is taken from the background maps, resulting in improved detection sensitivity as compared to the local detection step. The source list produced by *eboxdetect* was then used as input for *emldetect*. For all the sources detected with the sliding cell method this task performs a maximum likelihood *PSF* fit. In this way refined positions and fluxes for the sources were determined. As likelihood threshold for the detection, we adopted the value $det_{ml} = 6$ (about 3σ). Source detection summaries for each pointing in both the 0.5-2.0 keV and 0.4-0.6 keV bands are listed in Table 2 and Table 3 respectively.

The count rate-to-flux conversion factors for individual cameras were calculated using *XSPEC* and the *EPIC* response matrices generated by XMM-SAS tasks *rmfgen* and *arfgen*. The spectral model used was an intrinsic power law $\Gamma = 1.52$ affected by Galactic Neutral Hydrogen (*NH*). The individual conversion factors are listed in Table 4. The total conversion factor (*CF*) was calculated using the exposure times for *MOS1*, *MOS2*, and *PN*, and the conversion factors for the three instruments, *CFMOS1*, *CFMOS2*, and *CFPN* following the formula:

$$\frac{T_{TOT}}{CF} = \frac{T_{MOS1}}{CF_{MOS1}} + \frac{T_{MOS2}}{CF_{MOS2}} + \frac{T_{PN}}{CF_{PN}}, \quad (1)$$

where $T_{TOT}=(T_{MOS1}+T_{MOS2}+T_{PN})$. The source flux is then straightforward:

$$F_X = CF \times CR. \quad (2)$$

We generated sensitivity maps for each X-ray field and energy band, which contains the faintest flux at which a source can be detected at the assumed level of significance above the local background. The “sky coverage” defines the area of the sky covered down to a given flux limit, as a function of the flux. Due to the telescope vignetting and the increase in the size of the *PSF* in the outer regions of the detector, the sensitivity decreases toward the outer detector region. The sky coverage at a given flux was then obtained by adding up the contribution of all detector regions with a given flux limits. Figure 2 shows the average sky coverage for all pointing in the 0.5-2.0 keV and 0.4-0.6 keV bands.

3. Results

3.1. LogN-LogS and Total Flux from Discrete Sources

The cumulative logN-logS distribution (shown in Figure 3) for all the observations has been computed by summing up the contribution of each source, weighted by the area in which the source could have been detected, following the formula:

$$N(> S) = \sum_{i=1}^{N_s} \left(\frac{1}{\Omega_i} \right) \text{deg}^{-2}, \quad (3)$$

where N_s is the total number of detected sources in the field with flux greater than S and Ω_i is the sky coverage associated with the flux of the i^{th} source. The variance of the source number counts is then defined as:

$$\sigma_i^2 = \sum_{i=1}^{N_s} \left(\frac{1}{\Omega_i} \right)^2, \quad (4)$$

Our result in the 0.5-2.0 keV energy band, is qualitatively similar to other surveys (e.g., in Figure 3 we show the fits of Giacconi et al. 2001, Mateos et al. 2008, Hasinger et al. 1998, and Mushotzky et al., 2000), however our sample seems consistently richer in faint sources. When we fit the data with a power law in the flux range 9.0×10^{-16} to 1.0×10^{-13} erg s⁻¹ cm⁻², the resulting best fit to the logN-logS is:

$$N(> S) = (119 \pm 10) S^{-1.17 \pm 0.08}, \quad (5)$$

where S is the flux in units of 10^{-14} erg s⁻¹ cm⁻².

To quantitatively compare our result with previous investigations we looked at the number of detected sources at the faint end, bright end, and middle point of the flux range covered by our investigation. We compared our results both with the previous Chandra surveys by Mushotzky et al. (2000) and Giacconi et al. (2001), and the XMM-Newton results by Baldi et al. (2002). At the faint end of our logN-logS plot, the number of sources detected by our investigation is 42% higher than the estimates of Mushotzky (2000) and Giacconi (2001) and 35% higher than the results of Baldi (2002). At brighter fluxes our results are consistent, within the errors, with both Chandra data and the XMM-Newton survey. At the middle of the logN-logS ($S = 10^{-14}$ cgs), the number of detected sources is 20% higher than the Chandra results and 26% higher than XMM-Newton results. This discrepancy could arise from cosmic variation and/or by the different sample investigated. Baldi et al. (2002) used a single, large area of the sky, while in most other investigations,

e.g., Mushotzky (2000) and Hasinger (1998), the sources were identified and the logN-logS plot was limited to AGNs. While AGNs are expected to be the biggest contribution to X-ray point sources, our result, as confirmed by our spectral analysis reported in the next section, indicates that there is a significant component of non-AGN faint sources.

We also computed the resolved intensity of the detected sources by summing over the flux of each source divided by the inverse area over which the source would have been detected. The total intensity of the sources in all the pointings, in the flux range 7×10^{-16} to 10^{-14} erg s⁻¹ cm⁻² for the 0.5-2.0 keV band is $4.4 \pm 0.4 \times 10^{-12}$ erg s⁻¹ cm⁻² deg⁻² which corresponds to $\sim 36\%$ of the total *DXB* in the same band.

Figure 3 also shows the logN-logS distribution for sources in the 0.4-0.6 keV band, extending to a flux limit of 5.6×10^{-12} erg s⁻¹ cm⁻². Again, we fit the data with a power law in the flux range of 5.6×10^{-16} to 2.0×10^{-14} erg s⁻¹ cm⁻². The resulting best fit to the logN-logS is:

$$N(> S) = (21.7 \pm 4.9)S^{-1.16 \pm 0.15}. \quad (6)$$

The total intensity of the sources in all the pointings, in the flux range 2.0×10^{-16} to 2.0×10^{-14} erg s⁻¹ cm⁻² in the 0.4-0.6 keV band is $1.07 \pm 0.12 \times 10^{-12}$ erg s⁻¹ cm⁻² deg⁻² which corresponds to $\sim 25\%$ of the total *DXB* in that energy band. We note that all the sources identified in the 0.4-0.6 keV band are also identified in 0.5-2.0 keV band.

3.2. Energy spectra

We measured the average stacked spectrum of all the sources detected in the 0.5-2.0 keV and 0.4-0.6 keV bands. For this purpose, we use only *PN* data. The background spectrum was obtained using the event file of the total field of the same exposure, after removing the detected sources. The background was scaled by the ratio of the total exposure maps of the sources and the background. The *SAS* tasks *rmfgen* and *arfgen* were used to produce *EPIC* response matrices. We used *XSPEC*³ to compute the slope of a power law spectrum with average $NH=1 \times 10^{-20}$ cm⁻². The fit was over the energy range 0.5-7.5 keV (the *PN* spectrum shows a strong Cu-K line at 8.1 keV that should be avoided). We obtained a photon index of 1.75 ± 0.07 with normalization 7.24 ± 0.07 photons keV⁻¹ s⁻¹ cm⁻² sr⁻¹ and 1.93 ± 0.08 with normalization of 5.87 ± 0.06 photons keV⁻¹ s⁻¹ cm⁻² sr⁻¹ for all the sources detected in the 0.5-2.0 keV and 0.4-0.6 keV band respectively. Errors refer to 90% confidence levels. Both spectra with the best fit power law are shown in Figure 4. We note

³<http://heasarc.gsfc.nasa.gov/docs/xanadu/xspec/manual/manual.html>

that, as it may be expected, the spectrum of the sources identified in the 0.4-0.6 keV energy band is softer than that for the sources identified in the 0.5-2 keV band. The spectrum of the sources identified in the 0.5-2.0 keV band shows an excess of counts around 1 keV at the three sigma level ($\chi^2 = 26.7$, $n = 9$). The excess is well fitted with a zero redshift thermal component with temperature $T = 0.92$ keV, and emission measure $EM = 9 \times 10^{-5}$ cm $^{-6}$ pc, corresponding to a flux of 6.5×10^{-14} ergs s $^{-1}$ cm $^{-2}$ deg $^{-2}$. We attribute this thermal component to the contribution of stars in the Milky Way (Kashyap et al. 1992).

We also investigated the dependence of the spectral shape on the source brightness. This is particularly important as in most studies of the *DXB* only bright sources are detected and their properties are extended to faint ones. For this purpose we divided the detected sources into two groups, bright and faint, based on their flux. The threshold between the two groups was set to 2.0×10^{-15} erg s $^{-1}$ cm $^{-2}$. The spectrum of bright sources detected in the 0.5-2.0 keV band was well fitted in the energy range 0.5-7.5 with a power law of photon index 1.87 ± 0.07 and normalization 6.39 ± 0.06 photons keV $^{-1}$ s $^{-1}$ cm $^{-2}$ sr $^{-1}$ plus the $T = 0.92$ keV thermal component discussed above (see Figure 5). However, the spectrum of faint sources has an excess of counts below 0.7 keV and could not be fitted with a simple power law in that range (Figure 5). We performed a power law fit over the energy range 0.7-7.5 keV, obtaining a photon index $\Gamma = 1.05 \pm 0.03$ with normalization 0.70 ± 0.02 photons keV $^{-1}$ s $^{-1}$ cm $^{-2}$ sr $^{-1}$. Notice that the spectrum of faint sources does not show any significant thermal component around 1 keV.

We investigated the nature of the excess counts below 0.7 keV and here is a summary of our conclusions:

- The excess has a statistical significance of several sigmas ($\chi^2 = 217$, $n = 39$) and cannot be simply explained by statistical fluctuations.
- The excess was present in all pointings and is not due to a single anomalous source or target.
- We tried to fit the spectrum of faint sources with two power laws, one dominating above 1 keV, the other below 1 keV, but we could not improve the fit significantly.
- We also tried to fit the spectrum with a power law plus a thermal component (Figure 6) and the fit was greatly improved. Notice that, since the spectrum is the sum of the contribution from several sources, a fit with a single thermal component has, per se, limited significance. However, the goodness of the fit is a strong indication that the excess flux may be thermal in nature. The best fit parameter for the thermal component are $T = 2.1 \times 10^6$ K, redshift $z = 0.02$, and emission measure $EM = 0.00014$ cm $^{-6}$ pc,

for a total flux of the excess component equal to 8.5×10^{-14} ergs s⁻¹ cm⁻² deg⁻². The corresponding power law has photon index $\alpha = (1.03 \pm 0.02)$ and normalization 0.55 ± 0.02 photons keV⁻¹ s⁻¹ cm⁻² sr⁻¹. At this temperature the thermal component is expected to have a significant emission in O VII and O VIII, at a redshift that is practically indistinguishable from zero with the resolution of current satellites. The estimated emission from the excess thermal component is 0.19 LU (photons s⁻¹ cm⁻² sr⁻¹) and 0.06 LU for the O VII and O VIII respectively.

- We investigated the possibility that the excess is due to the contribution of Milky Way stellar sources. Kashyap et al. (1992) estimated the contribution to the diffuse soft X-ray background flux from Galactic stars at various energies ranging from 0.1 to ~ 5 keV. They found that stellar contribution at high Galactic latitudes is less than 3% for photon energies less than 0.3 keV, 3%-17% in the medium energy (~ 0.4 to ~ 0.9 keV) and 10%-30% in the high energy band (~ 0.8 -2.0 keV). Stars mainly have two temperature thermal spectra, since stellar corona emission is composed of two components namely a hot active component at nominal temperature $kT_a \sim 1$ keV (1.1×10^7 K) and a somewhat cooler quiescent component $kT_q \sim 0.3$ keV (3.5×10^6 K). In some stars only one thermal component is present, with a mean coronal temperature kT in the range [0.5, 0.8 keV] ($5.8 - 9.3 \times 10^6$ K; see e.g. Kashyap et al. 1992, Della Ceca et al. 2004, Lopez-Santiago et al. 2007). We have already discussed the excess thermal emission at $T = 0.92$ keV which we attribute to the stellar hot active component and we investigated the possibility that this lower temperature excess could be due to the cooler quiescent component. We fitted the excess with a thermal component at redshift zero and obtained a good fit with temperature $kT = 0.15$ keV (1.7×10^6 K) and emission measure $EM = 0.00016$ cm⁻⁶ pc. The total flux of the excess thermal component is compatible with what expected for stellar contribution, however, the best fit temperature is significantly smaller than the temperature range predicted by Kashyap et al. (1992). We also tried to fit the excess emission constraining the temperature values to the ranges described by Kashyap et al. (1992), using both one and two-temperature models, but we were unable to obtain a good fit.

In conclusion, we believe that, when we look at faint sources, in addition to the typical AGN contribution, there is also a significant contribution from a different class of sources with primarily thermal emission. Although the total flux of this contribution is consistent with stellar origin, its temperature is too low compared to typical stellar emission. This class of sources may also be explained by unresolved faint galaxies, galaxy clusters, and/or groups, and must be taken into account in the *DXB* budget.

We repeated the same investigation for sources detected in the energy band 0.4-0.6 keV.

The spectrum of bright (flux $\geq 10^{-15}$ erg s $^{-1}$ cm $^{-2}$) sources detected in the 0.4-0.6 keV band is well described with a power law fit of photon indexes 2.05 ± 0.02 with normalization of 4.74 ± 0.04 photons keV $^{-1}$ s $^{-1}$ cm $^{-2}$ sr $^{-1}$ (Figure 7). The spectrum of faint sources has a 3σ statistical significance for the thermal excess below 0.7 keV and could not be fitted with a simple power law in that range (Figure 7). We performed the power law fit over the energy range 0.7-7.5 keV, obtaining a photon index $\Gamma = 1.69 \pm 0.02$ with normalization of 1.02 ± 0.03 photons keV $^{-1}$ s $^{-1}$ cm $^{-2}$ sr $^{-1}$. In Figure 8 we show the spectrum of faint sources with overlapped the power law plus thermal component model. For the thermal component we used the same parameters as for the fit of faint sources identified in the soft band. The result of the spectral analysis in both bands is summarized in Tables 5 and 6.

4. The Diffuse X-ray Background

We combined our result with previous results to create a global picture of the *DXB* emission below 1 keV. As discussed before, in this energy range, the *DXB* is a mixture of the Galactic local bubble (*LB*) emission, solar wind charge exchange (*SWCX*), hot gas in the galactic halo (*GH*), and extragalactic flux from point sources and from intergalactic warm-hot gas (*WHIM*).

The ROSAT All Sky Survey (*RASS*) represents the most extensive study of the X-ray diffuse emission below 1 keV. Analysis of *RASS* data and subsequent observations has shown that there is significant spatial and temporal variation in the *DXB* emission (Snowden et al. 2000). The temporal variation is mostly attributable to the *SWCX*, while the spatial variation seems mostly due to *LB* and *GH* emission. An average over the whole sky indicates that the total diffuse X-ray emission in the 3/4 keV energy band is 3.04×10^{-12} ergs s $^{-1}$ cm $^{-2}$ deg $^{-2}$ (Kuntz et al. 2001). More recent work using XMM-Newton, Chandra, and Suzaku produces similar results. In particular, combining observations performed by Smith et al. (2005, 2006), Galeazzi et al. (2007), Henley et al. (2007, 2008), and Gupta et al. (2009) we obtained a total flux in O VII plus O VIII lines of $(3.1 \pm 0.8) \times 10^{-12}$ ergs s $^{-1}$ cm $^{-2}$ deg $^{-2}$ (12.5 ± 3.6 LU). Considering that the 3/4 keV band is dominated by these lines, the two results are in good agreement.

Moreover, the observations by Smith et al. (2005, 2006), Galeazzi et al. (2007), Henley et al. (2007, 2008), and Gupta et al. (2009) are shadow experiments and can be used to separate the *DXB* emission into two components, a foreground component consisting of *LB* and *SWCX* emission, and a background component consisting of *GH*, point sources, and *WHIM*. A typical shadow experiment consists of two observations, one in the direction of a high neutral hydrogen density cloud at a distance of 50 – 200 pc, the other in the

direction of a low neutral hydrogen column density region as close as possible to the cloud. As the cloud absorbs most of the background X-ray emission, the comparison of the two observations allows a clean separation between foreground and background. For example, in our previous investigation (Galeazzi et al. 2007) we used the high density, high latitude, neutral hydrogen cloud MBM20 which absorbs about 75% of the background in the energy range of 0.4-0.6 keV and a low-density region nearby, the Eridanus Hole, which absorbs only 8% of the background in the same energy range. Similarly, Smith et al. (2005, 2006) performed shadow observations in the direction of the cloud MBM12, and Henley et al. (2007, 2008) in the direction of a filament in the southern galactic emisphere. Combining all shadow investigations to account for spatial and temporal variations in the total diffuse flux, we found that $(30 \pm 12)\%$ (or 3.75 ± 1.3 LU in oxygen lines) of the diffuse emission is due to foreground sources, while $(70 \pm 12)\%$ (or 8.75 ± 1.3 LU in oxygen lines) is due to background sources.

Using the point sources identified in this investigation we can also set a lower limit to the diffuse emission due to usually unidentified point sources. Scaled to the 3/4 keV band, the cumulative flux of all point sources identified in this investigation corresponds to $(35 \pm 11)\%$ of the total *DXB* emission. We recently also performed an investigation of the *WHIM* emission using a statistical approach on the same targets used in this investigation (Galeazzi et al. 2009). In our investigation we found clear evidence of the emission from the *WHIM* and we quantified it as $(12 \pm 5)\%$ of the total *DXB* in the energy band 0.4-0.6 keV. A summary of the results with the contribution from each component is shown in Table 7.

5. Conclusions

We investigated the properties of point sources using data from the XMM-Newton public archive, focusing, in particular, on the properties below 1 keV and the contribution to the Diffuse X-ray Background. We looked at sources identified in two separate energy bands, a typical soft band 0.5-2 keV and a very soft one 0.4-0.6 keV. In the soft band, the sources detected in all the pointings at fluxes from 7.0×10^{-16} erg s⁻¹ cm⁻² to 1.0×10^{-13} erg s⁻¹ cm⁻² contribute a total flux of $(4.4 \pm 0.4) \times 10^{-12}$ erg s⁻¹ cm⁻² deg⁻², which corresponds to $\sim 36\%$ of the total CXB. The flux resolved in the very soft band from 2×10^{-16} to 2×10^{-14} erg s⁻¹ cm⁻² contributes a flux of $(1.07 \pm 0.12) \times 10^{-12}$ erg s⁻¹ cm⁻² deg⁻² corresponding to $\sim 25\%$ of the total CXB.

We obtained the cumulative spectra of all the sources identified in the two energy bands and also classified our sources using different flux thresholds. The threshold between the two groups was set to 2.0×10^{-15} and 10^{-15} erg s⁻¹ cm⁻² in the soft band and very soft band

respectively. A power law fit of the spectrum from bright sources in the range 0.5-7.5 keV using the average Galactic value of $NH = 1 \times 10^{-20} \text{ cm}^{-2}$ yields photon indexes of 1.77 ± 0.01 and 2.05 ± 0.02 for the sources detected in the soft band and very soft band respectively. When looking at faint sources, we found an excess flux around 0.5 keV in both bands that seems to be thermal in nature. We attribute the excess to a class of sources different from the typical *AGN* component, possibly unresolved galaxy clusters and/or groups, or coronal emission from stars in the Milky Way.

We would like to thank Dan McCammon and Steve Snowden for the very useful discussion and suggestions.

REFERENCES

- Baldi, A. & Molendi, S., et al. 2002, *ApJ*, 564, 190
- Cen, R. & Ostriker, J.P., et al. 1999, *ApJ*, 517, 31
- Della Ceca, R., Maccacaro, T., Caccianiga, A., et al. 2004, *A&A*, 428, 383
- Galeazzi, M., Gupta, A., Covey, K., & Ursino, E., 2007, *ApJ*, 658, 1081
- Galeazzi, M., Gupta, & Ursino, E., 2009, *ApJ*, in press
- Gendreau, K. C., et al. 1995, *PASJ*, 47, L5
- Giacconi, R. & Rossi, B. B., et al., 1962, *Phys. Rev. Lett.*, 9, 439
- Giacconi, R., et al. 2001, *ApJ*, 551, 624
- Gupta, A., et al., 2009, in preparation
- Hasinger, G., et al., 1998, *A&A*, 329, 495
- Henley, D. B., Shelton, R.L. & Kuntz, K. D., et al. 2007, *ApJ*, 661, 304
- Henley, D. B. & Shelton, R.L., et al. 2008, *ApJ*, 675, 335
- Kashyap, V., Rosner, R., Micela, G., Sciortino, S., Vaina, G. S. & Harnden, F. R., et al. 1992, *ApJ*, 391, 667
- Kuntz, K. D., Snowden, S. L. & Mushotzky, R. F., et al. 2001, *ApJ*, 548, L119

Lopez-Santiago, J., et al. 2007, A&A, 463, 165

Mateos, S., et al. 2008, A&A, 492, 51

McCammon, D., et al. 2002, ApJ, 576, 188

Mushotzky, R.F., Cowie, L.L., Barger, A.J., & Arnaud, K.A., et al. 2000, Nature, 404, 459

Read, A. M. & Ponman, T. J. 2003, A&A, 409, 395

Smith, R. K., et al., 2005, ApJ, 623, 225

Smith, R. K., et al., 2006, PASJ, 59, 141

Snowden, S. L., et al., 2000, ApJS, 128, 171

Ursino, E., & Galeazzi, M., 2006, ApJ, 652, 1085

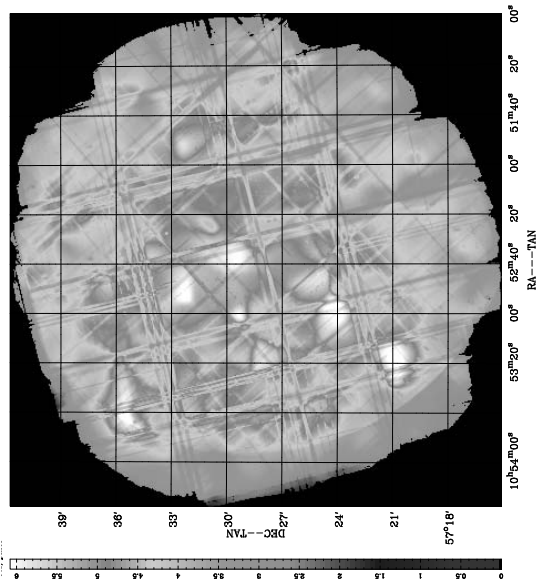


Fig. 1.— Background map derived as described in the text for the Lockman Hole target.

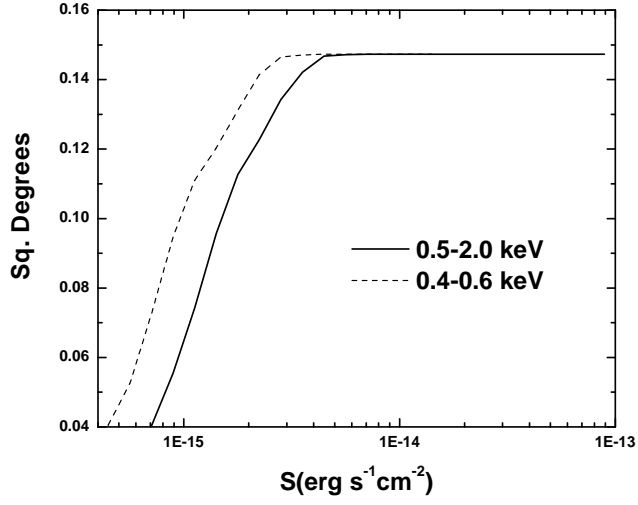


Fig. 2.— Average sky coverage for all pointing in the 0.5-2.0 keV and 0.4-0.6 keV bands.

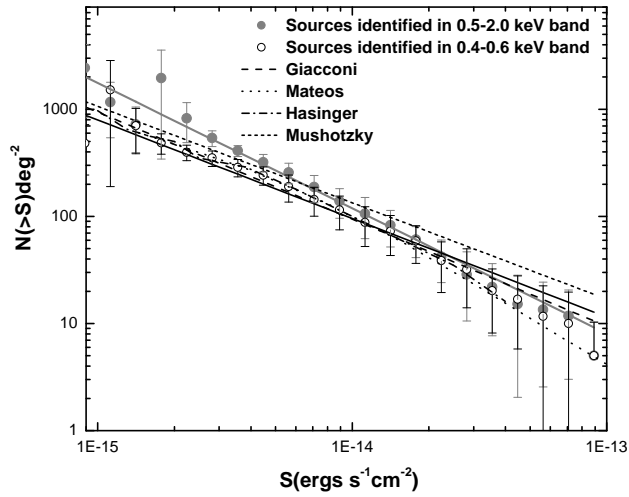


Fig. 3.— The average $\log N$ - $\log S$ in the 0.5-2 keV (full circles) and 0.4-0.6 keV (empty circles) bands for all targets used in this investigation. The black and gray curves represent the power law fit to the two experimental data sets respectively. The dotted line represents the best fit from Giacconi et al. (2001).

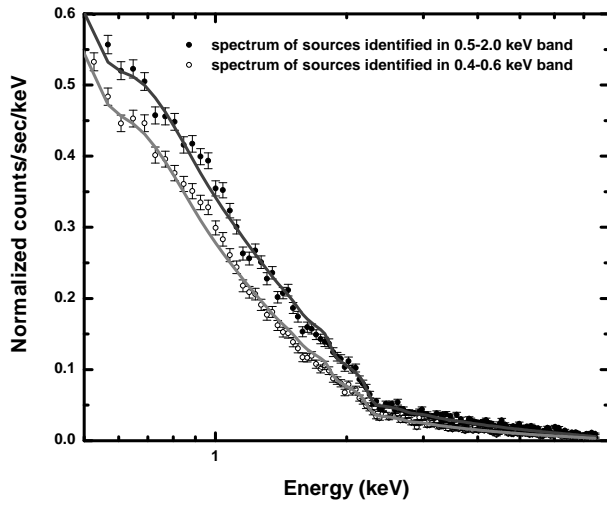


Fig. 4.— Average spectra of all the sources detected in the 0.5-2.0 keV (full black circles) and 0.4-0.6 keV (empty grey circles) bands. The dark grey and grey curve represents the power law fit in energy range 0.5-7.5 keV, for the two bands respectively.

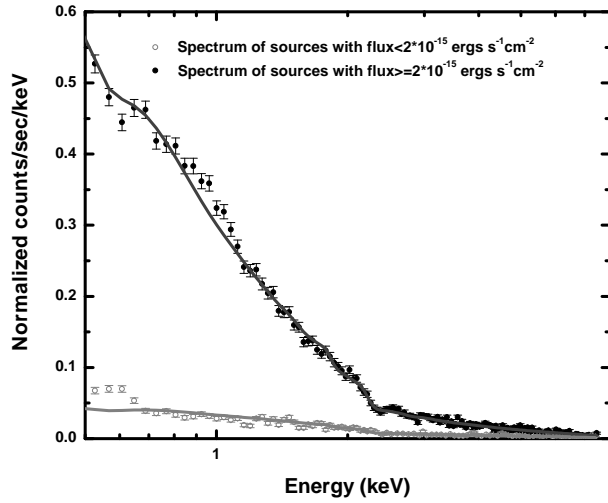


Fig. 5.— The average spectra of bright (full black circles) and faint (empty grey circles) sources detected in the 0.5-2.0 keV band. The dark grey and grey curves represent the power law fits for the bright and faint sources respectively. Note the soft excess at 0.5-0.65 keV for the faint sources.

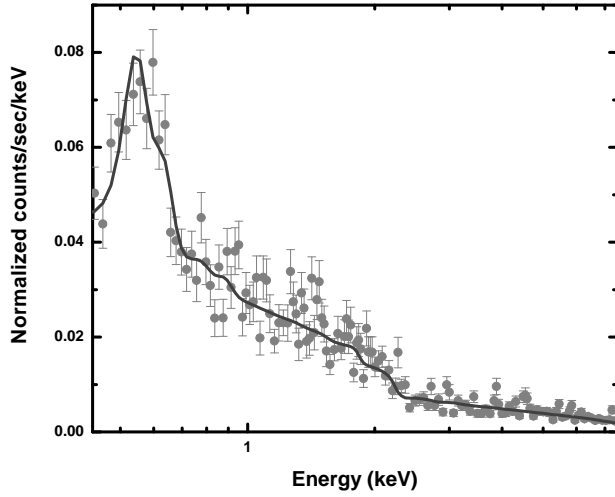


Fig. 6.— Average spectrum of faint sources fitted with an absorbed power law plus thermal component.

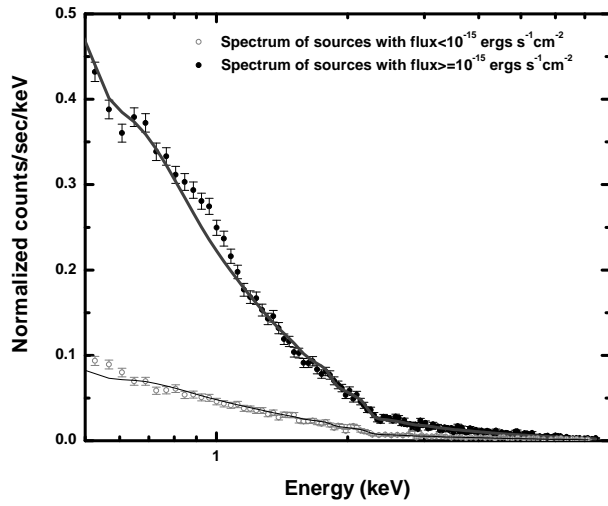


Fig. 7.— The average spectra of bright (full black circles) and faint (empty grey circles) sources detected in the 0.4-0.6 keV band. The dark grey and grey curves represent the power law fits for the bright and faint sources respectively.

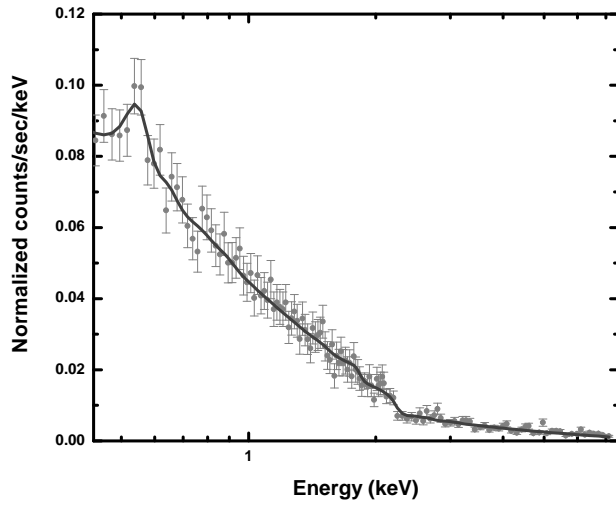


Fig. 8.— Average spectrum of faint sources fitted with an absorbed power law plus thermal component.

Table 1. Targets used in this investigation.

Target	l	b	NH(10^{20} cm^{-2})
Lockman Hole	149 16 48.1	53 08 45.9	0.7
Hubble Deep Field N	125 53 31.3	54 48 52.4	1.4
Deep Field 1334+37	85 37 22.5	75 55 16.4	0.8
Eridanus Hole	213 25 17.9	-39 04 25.6	0.86
AXAF Ultra deep F	223 34 36	-54 26 33.3	1.0

Table 2. Source detection in the 0.5-2.0 keV band.

Target	Exposure Time ^a	Minimum flux erg s ⁻¹ cm ⁻²	Sample		
	sec		Total	Faint ^b	Bright ^c
Lockman Hole	628945	2.34×10^{-16}	291	185	106
Hubble Deep Field	131751	7.18×10^{-16}	144	57	87
Deep Field 1334+37	165989	6.45×10^{-16}	159	60	99
Eridanus Hole	50230	9.96×10^{-16}	110	38	72
AXAF Ultra deep F	431618	31.9×10^{-16}	225	149	76

^aTotal exposure time from all available observations of the same target.

^bsources with flux $\leq 2.0 \times 10^{-15}$ erg s⁻¹ cm⁻²

^csources with flux $\geq 2.0 \times 10^{-15}$ erg s⁻¹ cm⁻²

Table 3. Source detection in the 0.4-0.6 keV band.

Target	Minimum detected flux erg s ⁻¹ cm ⁻²	Sample		
		Total	Faint ^a	Bright ^b
Lockman Hole	1.67×10^{-17}	143	99	44
Hubble Deep Field	4.02×10^{-16}	50	13	37
Deep Field 1334+37	3.84×10^{-16}	75	28	47
Eridanus Hole	4.48×10^{-16}	47	15	32
AXAF Ultra deep F	1.6×10^{-17}	108	78	30

^asources with flux $\leq 10^{-15}$ erg s⁻¹ cm⁻²

^bsources with flux $\geq 10^{-15}$ erg s⁻¹ cm⁻²

Table 4. Count-rate-to-flux conversion factors

EPIC Camera	0.5-2.0 keV	0.4-0.6 keV
<i>PN</i>	1.85×10^{-12}	1.48×10^{-12}
<i>MOS</i>	5.9×10^{-12}	6.18×10^{-12}

Note. — Count-rate-to-flux conversion factors for the individual EPIC cameras and energy bands, stated in units of $\text{erg s}^{-1} \text{cm}^{-2}$ for a rate of 1 counts s^{-1} . A photon-index power law of $\Gamma = 1.52$ affected by Galactic absorption of $1.0 \times 10^{20} \text{cm}^{-2}$ was assumed. Both *MOS* cameras were assumed to be identical.

Table 5. Spectral Fits on the 0.5-2.0 keV energy range

Sample	Objects	Γ^a	Flux ^b	Norm ^c	Reduced χ^2
Total	929	1.77 ± 0.01	4.8×10^{-12}	7.24 ± 0.07	1.3
Faint	489	1.05 ± 0.03	3.8×10^{-13}	0.70 ± 0.02	1.9
Bright	440	1.87 ± 0.01	4.8×10^{-12}	6.39 ± 0.06	1.1

^aPower law index of photon spectrum fit in the energy range of 0.5-7.5 keV

^bFlux of the sources in the energy range of 0.5-2.0 keV in units of $\text{erg s}^{-1}\text{cm}^{-2}\text{deg}^{-2}$

^cNormalization of power law fit in units of $\text{photons keV}^{-1} \text{s}^{-1} \text{cm}^{-2} \text{sr}^{-1}$

Table 6. Spectral Fits on the 0.4-0.6 keV energy range

Sample	Objects	Γ	Flux ^a	Norm	Reduced χ^2
Total	423	1.93 ± 0.01	1.1×10^{-12}	5.87 ± 0.06	1.1
Faint	233	1.69 ± 0.04	1.5×10^{-13}	1.02 ± 0.03	0.89
Bright	190	2.05 ± 0.02	8.6×10^{-13}	4.74 ± 0.04	0.94

^aFlux of the sources in the energy range of 0.4-0.6 keV in units of $\text{erg s}^{-1}\text{cm}^{-2}\text{deg}^{-2}$

Table 7. Components of the total diffuse X-ray emission in the 3/4 keV energy band

Total Luminosity = $6.25 \text{ keV s}^{-1} \text{ cm}^{-2} \text{ sr}^{-1}$	
Foreground	$(30 \pm 12)\%$
	SWCX Local Bubble
Background	$(70 \pm 12)\%$
	Galactic Halo WHIM $(12 \pm 5)\%$ Point Sources $\geq(35 \pm 11)\%$